



Power Electronic Systems
Laboratory

© 2021 IEEE

Proceedings of the 36th Applied Power Electronics Conference and Exposition (APEC 2021), June 14-17, 2021

High-Bandwidth High-CMRR Current Measurement for a 4.8MHz Multi-Level GaN Inverter AC Power Source

P. Niklaus,
D. Bortis,
J. W. Kolar

Personal use of this material is permitted. Permission from IEEE must be obtained for all other uses, in any current or future media, including reprinting/republishing this material for advertising or promotional purposes, creating new collective works, for resale or redistribution to servers or lists, or reuse of any copyrighted component of this work in other works.



Eidgenössische Technische Hochschule Zürich
Swiss Federal Institute of Technology Zurich

High-Bandwidth High-CMRR Current Measurement for a 4.8 MHz Multi-Level GaN Inverter AC Power Source

Pascal S. Niklaus, Dominik Bortis and Johann W. Kolar
 Power Electronic Systems Laboratory, ETH Zurich
 Physikstrasse 3, 8092 Zurich, Switzerland
 Email: niklaus@lem.ee.ethz.ch

Abstract—The control of very high switching frequency power electronic converter systems featuring latest generation wide bandgap (WBG) devices requires current measurements with a very high bandwidth (BW) to achieve high closed-loop control dynamics. One example is a ultra-high BW 4.8 MHz parallel-interleaved multi-level GaN inverter AC power source with a target output BW of 100 kHz. This work investigates the combination of state-of-the-art Hall-effect current sensors with a suitable high-frequency (HF) sensor to extend the BW of the commercially available current sensor by a factor of 20 – 50, i.e., up to 10 – 20 MHz. The main focus lies on a small form factor and a low realization effort. HF current sensors based on a Rogowski coil, an inductor integrated voltage sensing and a current transformer (CT) are analyzed and compared. Additionally, their respective performance limitations are highlighted. Furthermore, a precise combiner network to combine the low-frequency (LF) and HF signal is analyzed. The combiner circuit is designed in a way that component tolerances have no influence on the behavior in the transition frequency range from LF to HF. Thereby, also the immunity to Common-Mode (CM) disturbances, i.e., the high dv/dt occurring for the switching transitions of WBG semiconductors is considered. Finally, a hardware demonstrator featuring the two most promising current sensor approaches, i.e., the inductor voltage sensing and the CT, is presented and verified with comprehensive measurements in frequency and time domain. A BW from DC up to 35 MHz is measured. The realized sensors are further tested with a hardware prototype of the aforementioned AC power source switching 600 V at an effective switching frequency of 1.6 MHz. The measurements clearly reveal that both proposed sensor concepts are well suited for accurate measurements in fast switching converter systems with negligible additional volume.

Index Terms—Current Measurement, Hall Sensor, Rogowski Coil, Current Transformer, Inverter, Wide Bandgap Semiconductors, Multi-Level Converter, Ultra-High Bandwidth DC/AC Converter

I. INTRODUCTION

Modern power electronic converter systems tend to use latest wide bandgap (WBG) power semiconductors to allow higher switching frequencies (in the MHz-range), which in turn results in very power-dense system realizations. Besides a higher power density, MHz-range switching frequencies enable the realization of highly dynamic converter systems such as the GaN-based phase-modular 10 kW (per phase) AC power source with 100 kHz output bandwidth (BW) and an effective switching frequency of $f_{sw,eff} = 4.8$ MHz described in [1]. **Fig. 1 (a)** shows the proposed converter topology, a three-level ($N_{ser} = 3$) triple-interleaved ($N_{par} = 3$) flying capacitor converter (3L3) with the main specifications listed in **Fig. 1 (b)**. Each switching cell (two switches plus a flying capacitor) switches with 800 kHz, which results in a current ripple with a frequency of $f_{iLpp} = 1.6$ MHz in each of the three branch inductors L_{br} . The parallel-interleaved operation and the subsequent summation of the three inductor currents $i_{L,1...3}$ at the output filter capacitor node results in the effective switching frequency of 4.8 MHz. To achieve the demanded 100 kHz large signal output BW, closed-loop operation is required. A cascaded control scheme with a very fast inner

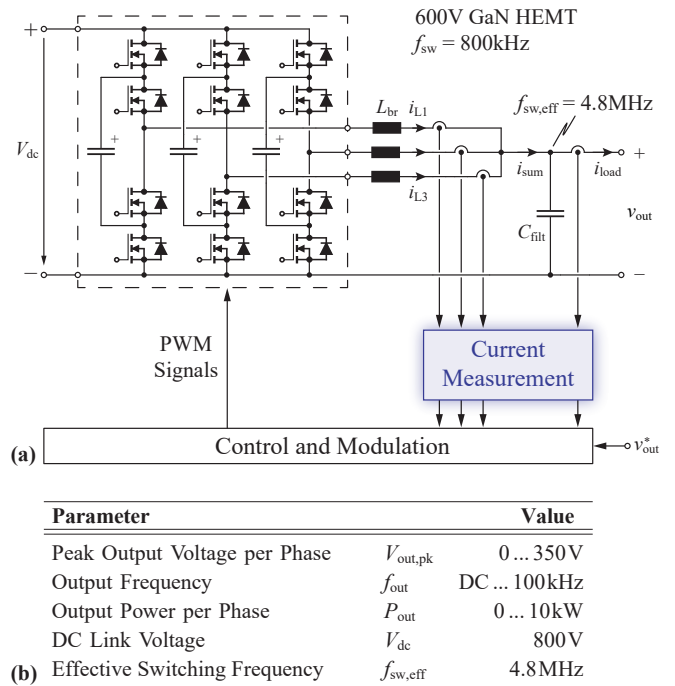


Fig. 1. (a) System overview of the 100 kHz large signal output voltage control bandwidth (BW) power amplifier realized as three-level triple interleaved (3L3) converter with GaN switches. **(b)** The main system specifications.

current controller and outer voltage controller including several feedforward paths turned out to be the most promising approach [2]. Wideband current and voltage measurements are required for proper operation of these fast controllers. The former is depicted in **Fig. 1 (a)** and is typically more challenging to realize in practice compared to voltage measurements, since most state-of-the-art current measurement principles are covering either DC and low frequencies (LF) < 1 MHz or high frequencies (HF) but not DC. The following requirements are considered for the target current measurement:

- DC capable and > 10 MHz BW to capture at least six harmonics (even and/or odd) of the 1.6 MHz triangular inductor currents,
- galvanic isolation to allow current measurements on a floating potential,
- no or very low added losses,
- current range of ± 40 A for the inductor current measurement and ± 65 A for the output current measurement with a sensitivity in the range of 20 – 30 mV/A to maximally utilize the full-scale voltage range of typical analog-to-digital converters (ADCs),
- high immunity to common-mode (CM) distortions resulting from the high dv/dt of WBG semiconductors,
- small form factor.

Most state-of-the-art commercial current sensors either rely on the Hall-effect [3], [4], feature a magneto-resistive element [5] or work based on the flux-gate principle [6]. They offer

very high precision, adequate sensitivity, high CM immunity, galvanic isolation and they are DC capable. Common to all is, however, the fundamental disadvantage of limited BW in the range of only 500 kHz to 1 MHz, which is at least one order of magnitude too low for the given application.

Although a commercial off-the-shelf solution would be desirable due to the ease of use and small form factor, unfortunately, no device that meets all the above requirements, particularly the BW, exists. To benefit from the aforementioned advantages of commercial sensors, an extension of the frequency range of a readily available commercial current sensor to make it suitable for the given application is desired.

The combination of a LF and HF current sensor has been comprehensively studied in literature. A typical approach is to use a Hall sensor in a open-loop [7]–[9] or closed-loop [10]–[12] configuration to measure the remaining magnetic flux density in the core of a gapped current transformer (CT). In the former case, the LF Hall sensor voltage is directly added to the output of the current transformer, whereas in the latter case a compensator injects a current into the CT secondary winding to nullify the magnetic flux in the core. The closed-loop approach has the advantage of linearizing the Hall sensor’s response but is fairly complex to realize. The common disadvantage of both approaches is the gap in the magnetic core to fit the Hall sensor, which complicates the manufacturing. Furthermore, there is a pronounced stray field in the vicinity of the air gap, which particularly for the open-loop configurations could distort the Hall sensor measurements due to parasitic voltage induction in the connecting leads [8], [10]. In [13], the Hall sensor and CT are operated independently of each other and combined using a dedicated combiner network. An alternative approach is presented in [14] where a Hall sensor in open-loop configuration is combined with a Rogowski coil [15]. The Rogowski coil measures the change in current and therefore needs a subsequent integration stage to obtain a signal that is proportional to the current [11], [16], [17]. This inherently limits the DC and LF response, which is added by the Hall sensor.

This paper comprehensively compares different possibilities to combine a LF and a HF current sensor regarding resulting performance, realization complexity and fundamental limitations. The analog combiner circuit to realize the LF and HF sensor combination is particularly emphasized with a detailed analysis of the frequency response. Furthermore, design guidelines are provided for a practical implementation of the presented current measurement solutions. The operation of the combiner circuit is independent of the utilized types of LF and HF sensors. Therefore, first, **Section II** discusses the design of the combiner circuit to combine the two sensor signals to achieve a flat wideband frequency response. Afterwards, **Section III** outlines three realization variants to extend the frequency range of commercial LF current sensors with emphasis on low realization effort and highlights the inherent limitations for each sensor type. In **Section IV**, the performance of the two most promising approaches is experimentally verified and compared using frequency and time domain measurements. Finally, the paper is concluded in **Section V**.

II. MEASUREMENT SYSTEM AND COMBINER CIRCUIT

Fig. 2 (a) shows the block diagram of the proposed measurement system including the combiner circuit, whose main purpose is to combine the signal v_{LF} of a LF sensor (ACS 733 Hall sensor in this case [4]) with its inherent low-pass characteristic (corner frequency f_{Hall}) with the signal v_{HF} of the HF extension (cf. **Section III**), which has an intrinsic high-pass characteristic (corner frequency $f_{c,HF}$). The combination

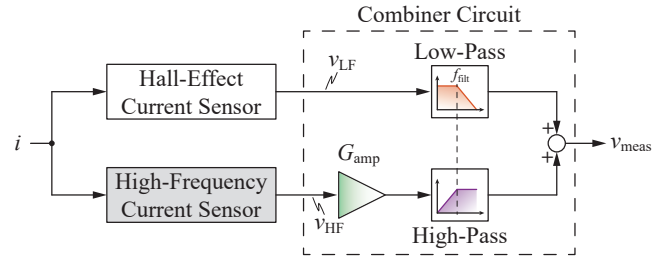


Fig. 2. Block diagram of the proposed current measurement system including the combiner circuit.

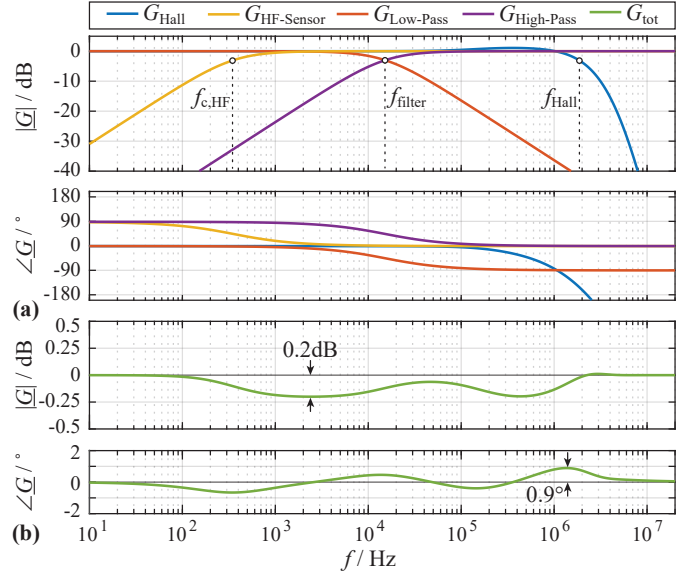


Fig. 3. (a) Magnitude and phase response of the LF Hall sensor (G_{Hall} , taken from the datasheet [4]) with $f_{Hall} \approx 1.8$ MHz, a HF current sensor ($G_{HF-Sensor}$) with $f_{c,HF} = 350$ Hz and the combiner network low-pass and high-pass filters with $f_{filter} = 15.2$ kHz. (b) Resulting total transfer function G_{tot} with its maximum magnitude and phase deviation of 0.2 dB and 0.9° , respectively.

is achieved with a combiner network having a low-pass characteristic with a corner frequency $f_{filt} = \omega_{filt}/(2\pi)$ for v_{LF} and a high-pass characteristic with the same corner frequency f_{filt} for v_{HF} , such that the summation of the two voltages equals

$$v_{meas} = v_{LF} \cdot \frac{1}{1 + s/\omega_{filt}} + v_{HF} \cdot G_{amp} \cdot \frac{s/\omega_{filt}}{1 + s/\omega_{filt}}. \quad (1)$$

To achieve a flat overall frequency response, the two voltages v_{LF} and v_{HF} must have a controlled magnitude and phase response. Therefore, a gain block (G_{amp}) is included in the HF path to equalize the gain of the LF and HF sensors. For low frequencies ($f \ll f_{filt}$) v_{meas} equals v_{LF} and for high frequencies ($f \gg f_{filt}$) equals $G_{amp} \cdot v_{HF}$. To define the transition from LF to HF signal solely with the combiner network, two necessary conditions have to be fulfilled:

- i) The LF and HF sensor must have the same sensitivity, i.e., the same gain v/i .
- ii) A sufficiently wide overlap of the frequency response of the LF and HF sensor is required, i.e., $f_{c,HF} < f_{filter} < f_{Hall}$.

Fig. 3 (a) exemplary shows the normalized individual sensor and filter transfer functions for $f_{c,HF} = 350$ Hz, $f_{Hall} = 1.8$ MHz (N.B.: not a first-order system; magnitude and phase response are taken from the Hall sensor datasheet [4]) and $f_{filter} = 15.2$ kHz together with (b) the resulting overall wideband transfer function $G_{tot} = v_{meas}/i$.

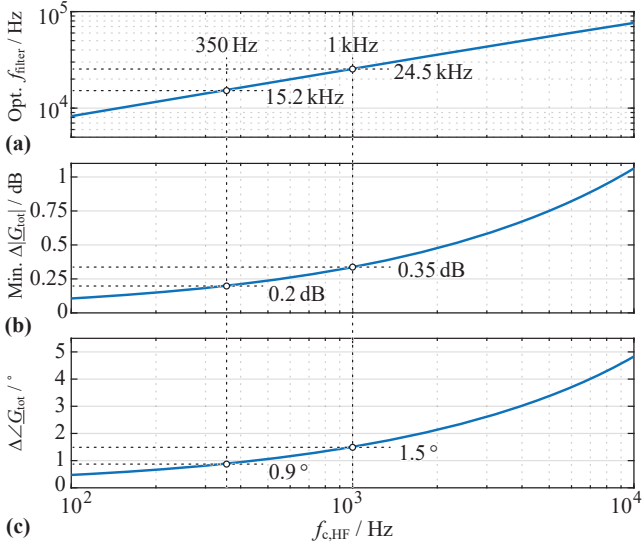


Fig. 4. (a) Optimal f_{filter} versus $f_{c,HF}$ for a given $f_{\text{Hall}} = 1.8$ MHz for minimum magnitude deviation $\Delta|G_{\text{tot}}|$. (b) Resulting magnitude deviation and (c) resulting phase deviation assuming the optimal f_{filter} . Highlighted are the values for $f_{c,HF} = 350$ Hz and 1 kHz, corresponding to the cases of the experimental verification.

The magnitude and phase deviations of G_{tot} over the full frequency range are 0.2 dB and 0.9° , respectively.

For every combination of $f_{c,HF}$ and f_{Hall} one can find the optimum value for f_{filter} , which results in a minimal magnitude deviation $\Delta|G_{\text{tot}}|$ in the overall transfer function G_{tot} , as shown in **Fig. 4 (a)**. **Fig. 4 (b)** depicts the resulting minimum magnitude deviation $\Delta|G_{\text{tot}}|$ and (c) the corresponding phase deviation $\Delta\angle G_{\text{tot}}$ for the given combination of f_{Hall} , f_{filter} and $f_{c,HF}$. Alternatively, f_{filter} could also be chosen to achieve minimum phase deviation, however, the results are very similar to **Fig. 4 (a)**. Generally, it is found that for a given Hall sensor frequency response a wider overlap of LF and HF sensor leads to a smoother total transfer function (less magnitude and phase deviation). As a rule of thumb, there should be at least one decade between $f_{c,HF}$ and f_{filter} and between f_{filter} and f_{Hall} . To keep the magnitude error below 0.5 dB (roughly 5%) and the phase error below 2° , $f_{c,HF}$ has to be chosen below 2 kHz (cf. **Fig. 4 (b)** and (c)). An accuracy in this range is considered sufficient, since in the given application the outer voltage controller can still correct small errors from the inner current controller, which, e.g., originate from slightly inaccurate measurements.

The combiner circuit is realized fully differentially to increase the immunity against CM distortions, e.g., from nearby switching actions. A simplified schematic is shown in **Fig. 5 (a)**. First, the single-ended LF sensor's output is converted to a fully differential signal. The HF sensor is realized differentially and amplified to increase the sensitivity (cf. **Fig. 2** and **Section III**). The low-pass and high-pass filters are realized as first-order passive filters with the components connected between the LF and HF signal buffer/amplifier, which inherently sets the corner frequency of the two filters to the same value, regardless of component tolerances. This mitigates a further source of magnitude and phase deviation. Moreover, the filters in the two differential signal lines do not need to be matched precisely thanks to the anyway present overlap of the LF and HF sensor frequency response, which means, even for a slight deviation from the optimal combiner frequency the overall transfer function is still sufficiently flat. The finalized hardware prototype of the combiner circuit is shown in **Fig. 5 (b)**. Apart from the bulky connectors required for testing purposes, a very compact realization is possible with dimensions of only 25 mm \times 22 mm (1.0 in. \times 0.87 in.).

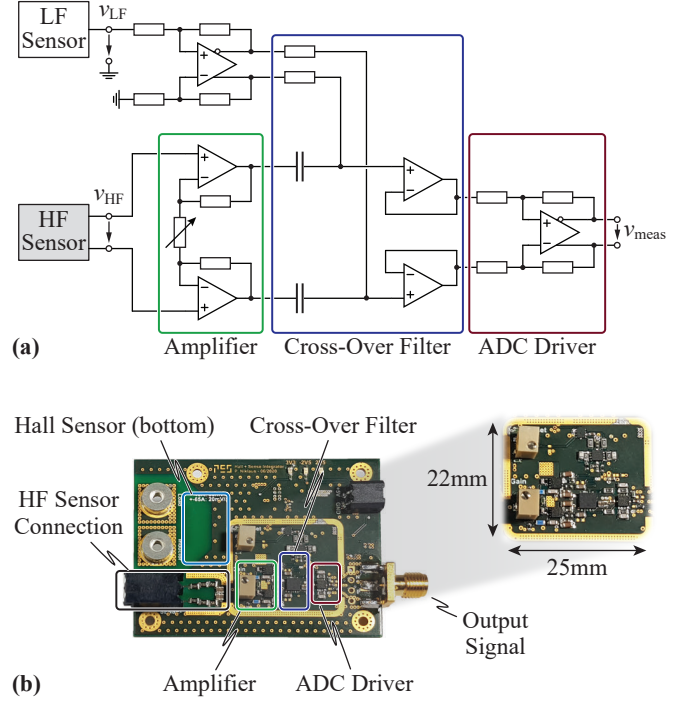


Fig. 5. (a) Simplified schematic of the fully differential combiner circuit and (b) picture of the realized hardware demonstrator for the performance evaluation with the individual blocks highlighted.

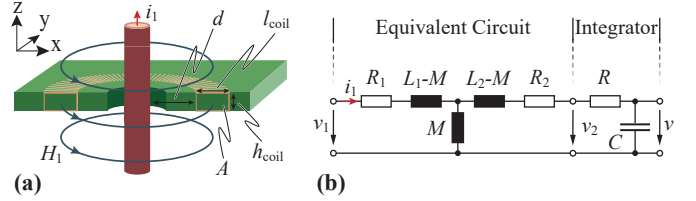


Fig. 6. (a) PCB-integrated circular Rogowski coil and (b) the corresponding equivalent circuit including self inductances L_1 and L_2 , mutual inductance M and winding resistances R_1 and R_2 as well as the passive integrator with R and C (galvanic isolation omitted).

The final design includes PCB mounted shields for improved immunity against external distortions, for example magnetic fields emerging from the loop formed by the connection of the main current to the Hall sensor.

III. HF MEASUREMENT PRINCIPLES

The basis of the wideband current sensor presented in this work is the commercially available open-loop Hall sensor ACS733, which has been selected because it offers a BW of > 1 MHz, galvanic isolation, integrated shielding for suppression of noise due to dv/dt transients, differential Hall sensing for immunity against external fields, comes in a small package and is proven to work in power electronics applications [4].

In the following, three concepts to extend the BW of the LF sensor are discussed, i.e., a Rogowski coil, a galvanically isolated inductive voltage sensing (IVS) and a current transformer (CT). The Rogowski coil and the CT are additional components that have to be added explicitly, whereas the IVS uses the already present core of the output inductor with an additional sense winding.

A. Rogowski Coil

As mentioned earlier, Rogowski coils generate a voltage v_2 that is proportional to the change in current (di_1/dt), where the proportionality factor is the mutual inductance M . In the frequency domain, the transfer function is

$$v_2 = s \cdot M \cdot i_1. \quad (2)$$

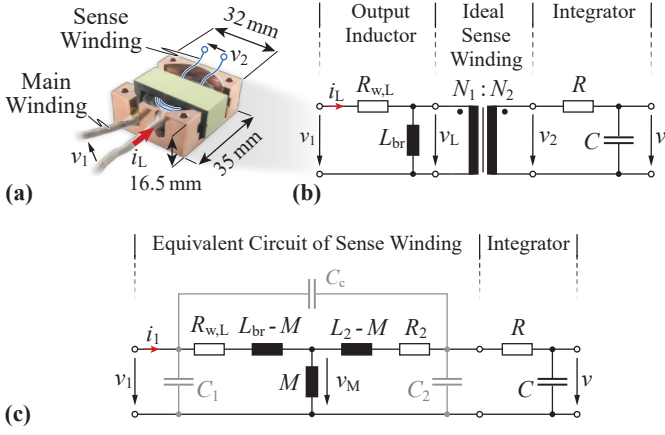


Fig. 7. (a) Picture of the realized output inductor with indicated sense winding and (b) the corresponding equivalent circuit for ideal coupling and including the passive integrator with R and C . (c) Equivalent circuit of the resulting transformer arrangement for non-ideal coupling including parasitic capacitances and omitted galvanic isolation.

The coil is either realized as helical winding wrapped around the conductor to be measured or as PCB integrated component, as illustrated in **Fig. 6 (a)** with the general equivalent circuit in **Fig. 6 (b)**. Due to the absence of a magnetic core the sensor behaves very linear but has a low mutual inductance M , which results in a rather low sensitivity. Combined with a passive integrator (RC low-pass filter, indicated in **Fig. 6(b)**) that terminates the coil with a high impedance, the resulting transfer characteristic in the frequency domain is

$$G_{\text{Rog}} = \frac{v}{i_1} = \frac{sM}{1 + sRC} = \frac{sM}{1 + s/(2\pi \cdot f_{c,\text{HF}})}. \quad (3)$$

This is a first-order high-pass filter with a corner frequency $f_{c,\text{HF}} = 1/(2\pi RC)$. To achieve a sufficiently flat combined transfer function, $f_{c,\text{HF}}$ has to be selected in the range of 1–2 kHz or even below (cf. **Section II**). For high frequencies ($f \gg f_{c,\text{HF}}$) the sensitivity is constant and equals $M/(RC)$. This directly shows the intrinsic trade-off between a low corner frequency (high RC product) and a high sensitivity (low RC product). To increase sensitivity without altering $f_{c,\text{HF}}$ a large mutual inductance M is required, which particularly on PCB integrated realizations results in a large coil size [16]. A mutual inductance of around 20 nH with a corner frequency of 1 kHz results in a sensitivity of only 125 $\mu\text{V}/\text{A}$. A gain stage can be placed directly after the integrator to increase the sensitivity (cf. **Fig. 2**) but due to the amplifier's finite gain-bandwidth product, the gain G_{amp} is typically constrained to values below 10. Therefore, a sensitivity of around 1.25 mV/A results, which is still too low for the desired application. A combination of the passive integrator with a more complex active integration stage allows a higher sensitivity for a given $f_{c,\text{HF}}$, since the passive integrator is not directly limiting the lower end of the frequency response as explained in detail in [18].

The BW of the Rogowski coil is implicitly limited by the coil's self-resonance frequency f_0 determined by the coil's self inductance L_2 and the parasitic coil capacitance (not included in the equivalent circuit in **Fig. 6 (b)**) [12]. For $f > f_0$, (2) is not valid anymore, since the coil behaves capacitively. This phenomenon is explained in more detail in the next section.

B. Galvanically Isolated Inductor Voltage Sensing

The mutual inductance and thus the sensitivity can be drastically increased when the Rogowski coil is wound on

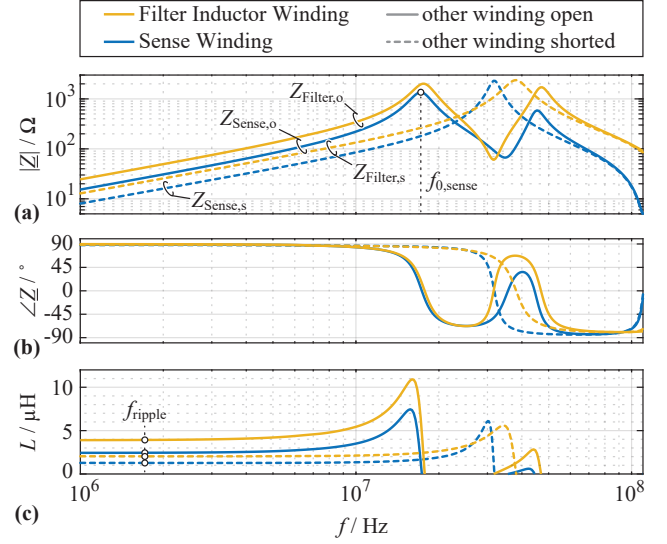


Fig. 8. Impedance measurements of the output inductor winding (yellow) and sense winding (blue) with the other winding open (continuous lines) or shorted (dashed lines). (a) Magnitude response, (b) phase response and (c) equivalent series inductance. Highlighted are the inductance values at the current ripple frequency of $f_{iL,\text{DP}} = 1.6$ MHz as well as the self-resonance frequency of the sense winding $f_{0,\text{sense}} = 17.2$ MHz.

a magnetic core. As indicated in **Fig. 1**, the output filter of the 3L3 converter has dedicated output (filter) inductors L_{br} , which are realized with a suitable high-frequency material (3F46) [1]. The inductive voltage is sensed with an additional sense winding on the already existing inductor core. This is equivalent to a transformer, whose secondary side (= sense winding) is loaded with a high-impedance RC integration circuit. Thus, the voltage v_2 is integrated according to (2) to determine the inductor current i_L as shown in **Fig. 7 (a)** and (b).

The basic principle is very similar to the non-isolated inductor voltage measurement, e.g., shown in [19]. The realization with an additional sense winding provides galvanic isolation and furthermore makes the measurement independent of the voltage drop across the inductor winding resistance $R_{w,L}$. Therefore, this method is hereinafter denoted as *galvanically isolated inductor voltage sensing (IVS)*.

The better sensitivity has to be traded for increased non-linearities due to the magnetic material (e.g., dependency of μ_r on frequency, current and temperature). Thanks to the air gap in the output inductor L_{br} , the material non-linearities have no significant impact on the inductor performance and thus do not alter the coupling of the transformer.

The equivalent circuit of **Fig. 7 (b)** is only valid for ideal coupling, hence the inductor voltage v_L is simply transformed by the turns ratio N_2/N_1 on the secondary side and with the subsequent integration with R and C the sensor sensitivity becomes

$$G_{\text{sense}} = \frac{v_{2,\text{int}}}{i_L} = \frac{N_2}{N_1} \frac{sL_{\text{br}}}{1 + sRC} \stackrel{f \gg 1/(2\pi RC)}{\approx} \frac{N_2}{N_1} \frac{L_{\text{br}}}{RC}. \quad (4)$$

For the case at hand, the output inductor winding consists of $N_1 = 6$ turns and the sense winding is realized with $N_2 = 4$ turns. In practice, the coupling is non-ideal (but significantly better compared to a classical Rogowski coil) and the equivalent circuit of **Fig. 7 (c)** applies. In this case, the mutual inductance M has to be determined, e.g., by impedance measurements and the sensitivity is determined with (3). Impedance measurements with open and shorted primary and secondary side (cf. **Fig. 8**) evaluated at $f = 1.6$ MHz reveal a mutual inductance of $M \approx 2.14 \mu\text{H}$ and correspond-

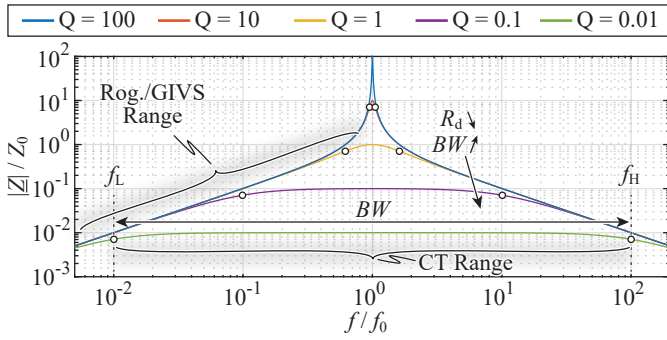


Fig. 9. Impedance of a Rogowski coil and/or IVS winding and/or CT secondary winding for different quality factors $Q = R_d/Z_0$. For a given resonance frequency f_0 the peaking reduces with lower Q (lower R_d). Highlighted are the operation range of the Rogowski coil and the IVS (range where Z increases with f) as well as the operation range of the CT (range where Z is flat).

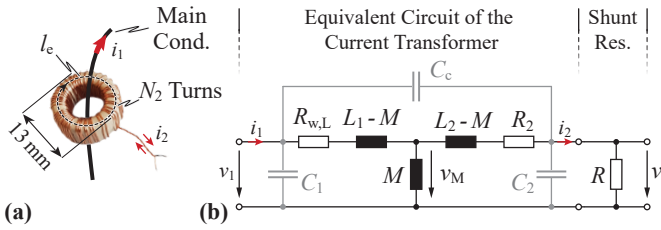


Fig. 10. (a) Picture of realized iron powder core current transformer (CT) with one primary and $N_2 = 50$ secondary turns and (b) the equivalent circuit including the low-ohmic burden resistor R .

ingly a sensitivity of 13.4 mV/A. Compared to the minuscule 125 μ V/A of the Rogowski coil this is an improvement by two orders of magnitude. Like a conventional Rogowski coil, the inductive voltage sensing only works below the self-resonance frequency $f_{0,\text{sense}} = 17.2$ MHz, determined by the parallel resonance between the self inductance L_2 and the equivalent capacitance $C_2 \parallel \frac{C_c C_1}{C_c + C_1}$ of the sense winding (cf. **Fig. 7 (c)** and **Fig. 8**). The latter is relatively large due to the compact winding construction, which is possible thanks to the low required number of turns as an effect of the better coupling with the magnetic core. However, the upper BW limitation is still perfectly within the range indicated above and is sufficient for the desired application as verified with measurements in **Section IV**.

The inductor voltage is switched between ± 400 V and due to the low turns ratio N_2/N_1 , the sensed voltage v_2 is in the order of several tens to hundreds of volts. Therefore, it is not possible to damp the resonance with a damping resistor R_d parallel to C_2 (cf. **Fig. 7 (c)**) due to the large inherent losses.

C. Current Transformer

As it is the case in a classical Rogowski coil, the BW of the IVS is inherently limited by the self-resonance frequency of the sense winding. To prevent peaking in the frequency response, Rogowski coils often include a damping resistor R_d , which effectively damps the resonance as qualitatively indicated in **Fig. 9**. The reduced load impedance (compared to the high impedance integrator) w.r.t to the characteristic impedance $Z_0 = \sqrt{L/C}$ lowers the quality factor Q and therefore, the peak at the resonance frequency f_0 becomes flatter. As mentioned above, for the IVS this is not possible due to the high losses, since the required R_d to prevent peaking is around Z_0 ($Q \approx 1$), which is typically in the order of several hundred ohms.

A current transformer (CT) as shown in **Fig. 10** solves this problem, since it usually features only a single primary turn N_1 and a high number of secondary turns N_2 . Therefore, the

inserted series impedance in the main current path is very low and the CT can be loaded with a low-ohmic burden resistor R . A consequence thereof is that no integration stage is required, since the CT outputs a voltage directly proportional to the primary current i above its corner frequency

$$f_{c,\text{HF}} = f_L = \frac{1}{2\pi} \cdot \frac{R_2 + R}{L_2} \quad (5)$$

as nicely shown, e.g., in [12] and in **Fig. 9**. R_2 and L_2 are the resistance and self inductance of the secondary winding, respectively. The CT requires a dedicated small (iron powder) core, which adds a certain volume to the system. It is, however, necessary in cases where no dedicated inductor for voltage sensing is present, e.g., for the measurement of the load current (cf. **Fig. 1**) or in cases where the filter inductance is realized as stray inductance of a common-mode choke.

Fig. 10 (b) shows the equivalent circuit of the current transformer, which apart from the low-ohmic burden resistor instead of the integration stage is identical to the one of the Rogowski coil and/or sense winding. The circuit parameters, however, cannot be determined with the classical open and short circuit impedance measurements, due to the typically large turns ratio. Particularly the short circuit impedance measurement is largely dominated by parasitics of the measurement setup. Instead, the voltage or current transfer ratio can be used together with primary and secondary open circuit impedance measurements to fully determine the equivalent circuit parameters. Please note, that due to the high turns ratio, the elements $(L_1 - M)$ and/or $(L_2 - M)$ in the equivalent circuit representing the leakage of the transformer can become negative [20]. The circuit, however, is still physically valid. With **Fig. 10 (b)** the CT transfer ratio G_{CT} equals

$$G_{\text{CT}} = v/i_1 = R \cdot \frac{sM/(R_2 + R)}{1 + sL_2/(R_2 + R)} \quad (6)$$

where the turns ratio N_1/N_2 is implicitly included in the circuit elements. For frequencies above $f_{c,\text{HF}}$ (cf. (5)) (6) reduces to $R \cdot M/L_2$, i.e., there is a current division between the mutual inductance and the path through the secondary burden resistor. For ideal coupling, G_{CT} simplifies to

$$G_{\text{CT,ideal}} = R/N_2. \quad (7)$$

Any leakage inductance leads to a gain error in G_{CT} , which has to be corrected during calibration. Based on the desired sensitivity, the ratio R/N_2 is directly given.

To avoid the previously mentioned disadvantages accompanied with a gapped current transformer, the DC and LF flux are not compensated in the CT and a standard toroidal iron powder core is used, which in addition is beneficial to minimize the leakage inductance [21]. When using a standard toroidal core without an air gap, it has to be ensured that the core does not saturate, since also the DC and LF current passes through it. In contrast to [13], which combines a commercial Hall sensor with a commercial CT, a higher measurement range and BW is possible with a custom designed CT. For an impressed current i_1 the magnetic flux density B in the core can be calculated using Ampère's law

$$B = \mu_0 \cdot \mu_r \cdot \frac{i_1}{l_e} \quad (8)$$

($N_1 = 1$) where μ_0 and μ_r denote the vacuum and relative material permeability and l_e the length of the magnetic path in the core. To minimize $f_{c,\text{HF}}$ for a smooth transition between LF and HF sensor (cf. **Section II**), according to (5),

$$L_2 = \mu_0 \cdot \mu_r \cdot N_2^2 \cdot \frac{A_e}{l_e} \quad (9)$$

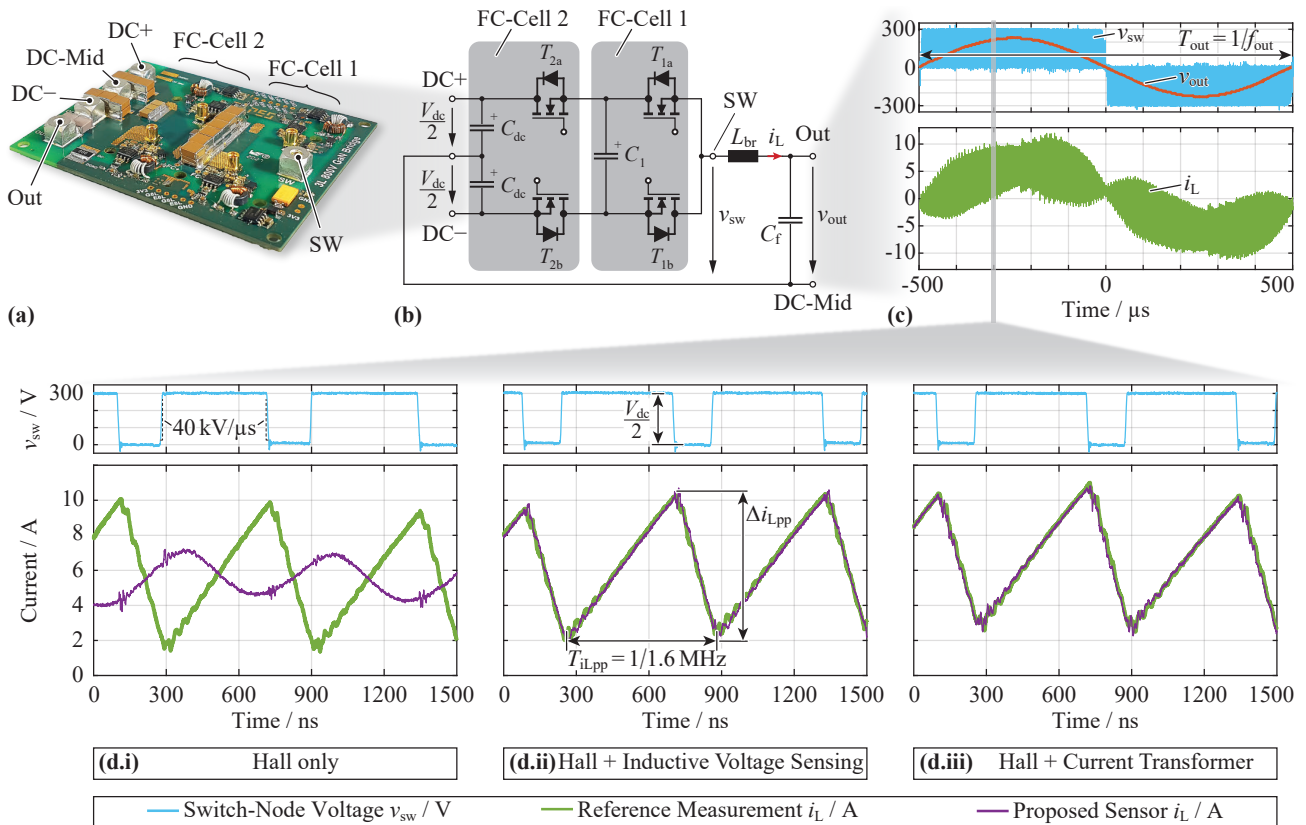


Fig. 13. Performance verification of the proposed sensor in time-domain using (a) a hardware demonstrator of (b) a single three-level branch of the GaN 3L3 AC power source operated with $V_{dc} = 600$ V and an effective switching frequency of $f_{sw} = 1.6$ MHz at an output power $P_{out} \approx 1$ kW. (c) shows the switch-node voltage v_{sw} (cyan curves), the output voltage v_{out} (post processing, red curve) and the reference measurement for the inductor current i_L (TCP0030A current probe [24], green curves) over one fundamental period $T_{out} = 1/f_{out} = 1$ ms (100 μ s/div). Zoomed views (300 ns/div) of two switching periods show the comparison of the reference measurement with (d.i) only the Hall sensor without BW extension, (d.ii) the Hall sensor and the inductive voltage sensing and (d.iii) the Hall sensor and the current transformer (purple curves).

commercial Hall sensor and is achieved by simply placing a small additional winding on the already present magnetic core (negligible volume and realization complexity). f_x in this case denotes the frequency at which the amplitude is +3 dB above the nominal value. A zoomed view, which shows the flatness of the magnitude response is further depicted in Fig. 12 (a).

The extension of the Hall sensor with the CT allows for an even higher BW, i.e., an improvement of a factor > 20 compared to the Hall sensor, but the transfer function shows a larger deviation from the nominal value (0.5 dB, i.e., around 5%). In addition, the higher performance is traded for the additional required volume of ≈ 1 cm³, which is, however, almost negligible in the overall converter system. As already mentioned earlier, for the given application a small error in the current measurement is not a big concern, particularly at low frequencies in the kHz range, since there will be an outer voltage control loop with integrating behavior, which corrects the measurement error. Please note, that the Hall sensor alone (blue curve in Fig. 12) is only measured using the LF power amplifier, hence its frequency response (dashed line in Fig. 12) is only valid up to 3 MHz. It could be verified, however, that there are some internal parasitic couplings in the Hall sensor, which lead to an increase of its response at high frequencies ($f > 10$ MHz).

B. Time-Domain Behavior

To verify the time-domain behavior, a hardware demonstrator of one three-level branch of the GaN 3L3 AC power source with $V_{dc} = 600$ V is used to generate a reference inductor current i_L . It has a fundamental frequency component of 13 A peak-to-peak at $f_{out} = 1/T_{out} = 1$ kHz (= output current) and a superimposed ripple with a frequency $f_{iLpp} = 1.6$ MHz.

Fig. 13 (a) and (b) show the hardware demonstrator and the corresponding circuit, which is supplied with a split DC link $V_{dc}/2 = 300$ V. Fig. 13 (c) depicts waveforms of the resulting switch-node voltage v_{sw} , reconstructed output voltage v_{out} (filtered in post-processing) and inductor current i_L over one fundamental period T_{out} . Both voltages are referred to the DC mid-point. Zoomed views in Fig. 13 (d) show the comparison of the reference current measurement using a Tektronix TCP0030A 120 MHz BW current probe [24] (green curves) with (d.i) the Hall sensor alone, (d.ii) the Hall sensor extended with the inductive voltage sensing and (d.iii) the Hall sensor extended with the CT (purple curves) in an exemplary time interval of two switching periods in the current ripple with $\Delta i_{Lpp} \approx 8$ A peak-to-peak. Both, the proposed sensor and the current probe are placed after the inductor to reduce the effect of fast voltage transients at the switch-node ($dv/dt \approx 40$ kV/ μ s). Furthermore, the output of the proposed sensor is calibrated for offset and gain errors. Evidently, both sensor concepts accurately replicate the 1.6 MHz triangular current ripple. Therefore, the BW is in both cases enough to capture the relevant harmonic content. No significant distortions during the switching events of the power stage are visible. It can be clearly seen, however, that the Hall sensor alone is clearly not enough to get an adequate representation of the inductor current as indicated with the quasi-sinusoidal shape instead of a triangular one, the too small amplitude and the large phase-shift to the reference measurement. It could be verified that the CM robustness, i.e., the susceptibility to CM distortions from high dv/dt transients, is significantly better with the fully differential realization of the combiner circuit compared to a single-ended implementation.

In conclusion, it could be verified that the BW of both approaches is sufficient to accurately measure the 1.6 MHz triangular ripple current. The IVS has lower additional volume (no additional magnetic core) and low realization effort (few turns of sense winding). The CT adds around 1 cm³ due to the magnetic core and the realization is relatively complex due to the toroidal core. However, it is beneficial in situations where no dedicated inductor is present and the IVS is not usable.

V. CONCLUSION

This paper analyzes approaches to extend the bandwidth (BW) of a commercially available Hall-effect current sensor beyond 10 MHz. The aim is to implement a wideband current measurement for closed-loop control of a ultra-high BW AC power source with an effective switching frequency $f_{sw,eff} = 4.8$ MHz employing wide bandgap GaN semiconductors. It is shown that an existing output inductor can be equipped with a sense winding to obtain the inductor current by integration of the inductive voltage drop (*galvanically isolated inductor voltage sensing*, IVS). This is advantageous for power dense applications, since no additional magnetic element has to be placed. In case no dedicated inductor is present, e.g., for the output current measurement, a small current transformer (CT) with an ungapped toroidal core can be used to extend the Hall sensor BW. A fully differential combiner circuit with an optimized combiner filter allows a smooth transition between the Hall sensor (low-frequency, LF) and the high-frequency (HF) sensor. The transition is independent of component tolerances of the filter elements provided there is a sufficient overlap of the LF and HF sensors in their frequency response. Therefore, no trimming of filter corner frequencies is required. A very compact realization of the combiner circuit with a PCB area of only 25 mm × 22 mm (1.0 in. × 0.87 in.) is possible. Comprehensive experimental verification proofs that a 1.6 MHz current ripple is accurately represented with both approaches. The realization with the CT features a higher BW (35 MHz) compared to the inductor voltage sensing (10 MHz), however, the magnitude response in frequency domain shows a slightly higher deviation from the ideal flat response (0.5 dB compared to 0.3 dB). Based on these findings it makes most sense to adopt the galvanically isolated inductor voltage sensing for the measurement of the three output (filter) inductor currents and use the CT only for the load current measurement. There, the higher BW of the CT is beneficial to quickly react to instantaneous load changes by means of a load current feed forward.

REFERENCES

- [1] P. S. Niklaus, J. A. Anderson, D. Bortis, and J. W. Kolar, "Ultra-high bandwidth gan-based class-d power amplifier for testing of three-phase mains interfaces of renewable energy systems," in *8th International Conference on Renewable Energy Research and Applications (ICR-ERA)*, 2019, pp. 615–622.
- [2] F. Krismer, V. N. Behrunani, P. S. Niklaus, and J. W. Kolar, "Optimized cascaded controller design for a 10 kw / 100 khz large signal bandwidth ac power source," in *Proc. of the IEEE Energy Conversion Congress and Exposition (ECCE)*, 2020, pp. 5669–5676.
- [3] E. H. Hall, "On a new action of the magnet on electric currents," *American Journal of Mathematics*, vol. 2, no. 3, pp. 287–292, 1879. [Online]. Available: <http://www.jstor.org/stable/2369245>
- [4] Allegro Microsystems, "Acs733 – datasheet," 2020, accessed on 11.02.2021. [Online]. Available: <https://www.allegromicro.com/-/media/files/datasheets/acs732-3-kl-a-datasheet.ashx>
- [5] Sensitec GmbH, "Cfs1000 – datasheet," 2020, accessed on 11.02.2021. [Online]. Available: https://www.sensitec.com/fileadmin/sensitec/Service_and_Support/Downloads/Data_Sheets/CFS1000/SENSITEC_CFS1000_DSE_05.pdf
- [6] LEM International SA, "High precision current transducers," 2011, accessed on 11.02.2021. [Online]. Available: <https://www.lem.com/en/file/5619/download>
- [7] L. Dalessandro, N. Karrer, and J. W. Kolar, "High-performance planar isolated current sensor for power electronics applications," *IEEE Transactions on Power Electronics*, vol. 22, no. 5, pp. 1682–1692, 2007.
- [8] L. Ghislanzoni and J. A. Carrasco, "A dc current transformer for large bandwidth and high common-mode rejection," *IEEE Transactions on Industrial Electronics*, vol. 46, no. 3, pp. 631–636, 1999.
- [9] G. Laimer and J. W. Kolar, "Wide bandwidth low complexity isolated current sensor to be employed in a 10 kw/500 khz three-phase unity power factor pwm rectifier system," in *Proc. of the 33rd IEEE Power Electronics Specialists Conference (PESC)*, 2002, pp. 1065–1070 vol.3.
- [10] J. A. Carrasco, E. Sanchis-Kilders, D. Ramirez, and E. J. Dede, "Improved magnetic coupled current sensing techniques [space power applications]," in *Proc. of the 27th IEEE Power Electronics Specialists Conference (PESC)*, 1996, pp. 829–834 vol.1.
- [11] B. Mammano, "Current sensing solutions for power supply designers," Unirode Corp., 1997.
- [12] P. Hofer-Noser and N. Karrer, *Hochdynamische Stromerfassung in der Leistungselektronik*. Springer Berlin Heidelberg, 2006, pp. 849–883.
- [13] B. Ulrich, "Open-source wideband (dc to mhz range) isolated current sensor," *HardwareX*, vol. 5, 2019. [Online]. Available: <http://www.sciencedirect.com/science/article/pii/S2468067218300592>
- [14] N. Karrer and P. Hofer-Noser, "A new current measuring principle for power electronic applications," in *Proc. of the 11th IEEE International Symposium on Power Semiconductor Devices and ICs (ISPSD)*, May 1999, pp. 279–282.
- [15] W. Rogowski and W. Steinhaus, "Die Messung der magnetischen Spannung (in German)," *Archiv f. Elektrotechnik*, vol. 1, no. 4, pp. 140–150, 1912.
- [16] H. L. Votzi, M. Vogelsberger, and H. Ertl, "Low-cost current sensor for power capacitors based on a pcb rogowski-coil," in *Proc. of the International Exhibition & Conference for Power Electronics, Intelligent Motion, Power Quality (PCIM)*, 2011.
- [17] B. Carsten, "The proximity current probe; obtaining wideband current waveforms in thick film and printed circuit conductors," in *Proc. of the 1st High Frequency Power Conversion Conference (HFPC)*, May 1989.
- [18] J. Pettinga and J. Siersema, "A polyphase 500 kA current measuring system with Rogowski coils," *IEE Proceedings B Electric Power Applications*, vol. 130, no. 5, p. 360, 1983.
- [19] E. Dallago, M. Passoni, and G. Sassone, "Lossless current sensing in low-voltage high-current dc/dc modular supplies," *IEEE Transactions on Industrial Electronics*, vol. 47, no. 6, pp. 1249–1252, 2000.
- [20] T. Guillod, F. Krismer, and J. W. Kolar, "Magnetic equivalent circuit of mf transformers: modeling and parameter uncertainties," *Springer Nature, Electrical Engineering*, vol. 100, no. 4, pp. 2261–2275, 2018.
- [21] E. Laboure, F. Costa, and F. Forest, "Current measurement in static converters and realization of a high frequency passive current probe (50 a-300 mhz)," in *Proc. of the 5th European Conference on Power Electronics and Applications*, 1993, pp. 478–483.
- [22] Micrometals, "T50-70b – datasheet," 2019, accessed on 11.02.2021. [Online]. Available: <https://datasheets.micrometals.com/T50-70B-DataSheet.pdf>
- [23] Omicron Lab, "Bode 100 – user manual," 2021, accessed on 11.02.2021. [Online]. Available: https://www.omicron-lab.com/fileadmin/assets/Bode_100/Manuals/Bode-100-User-Manual-ENU10060507.pdf
- [24] Tektronix, Inc., "Tep0030a – datasheet," 2017, accessed on 11.02.2021. [Online]. Available: <https://download.tek.com/datasheet/TCP0030A-Current-Probe-Datasheet-51W1904210.pdf>
- [25] S. Ziegler, R. C. Woodward, H. H. Iu, and L. J. Borle, "Current sensing techniques: a review," *IEEE Sensors Journal*, vol. 9, no. 4, pp. 354–376, 2009.
- [26] Texas Instruments, "Opa859 – datasheet," 2018, accessed on 11.02.2021. [Online]. Available: <https://www.ti.com/lit/ds/symlink/opa859.pdf>